PHYSICAL REVIEW C **77**, 024912 (2008)

Cold nuclear matter effects on J/ψ production as constrained by deuteron-gold measurements at $\sqrt{s_{NN}} = 200$ GeV

A. Adare,[10] S. S. Adler,[5] S. Afanasiev,[24] C. Aidala,[11] N. N. Ajitanand,[50] Y. Akiba,[25,44,45] H. Al-Bataineh,[39] J. Alexander,[50]
A. Al-Jamel,[39] K. Aoki,[29,44] L. Aphecetche,[52] R. Armendariz,[39] S. H. Aronson,[5] J. Asai,[45] E. T. Atomssa,[30] R. Averbeck,[51]
T. C. Awes,[40] B. Azmoun,[5] V. Babintsev,[20] G. Baksay,[16] L. Baksay,[16] A. Baldisseri,[13] K. N. Barish,[6] P. D. Barnes,[32]
B. Bassalleck,[38] S. Bathe,[6,35] S. Batsouli,[11,40] V. Baublis,[43] F. Bauer,[6] A. Bazilevsky,[5,45] S. Belikov,[5,*] R. Bennett,[51]
Y. Berdnikov,[47] A. A. Bickley,[10] M. T. Bjorndal,[11] J. G. Boissevain,[32] H. Borel,[13] K. Boyle,[51] M. L. Brooks,[32] D. S. Brown,[39]
N. Bruner,[38] D. Bucher,[35] H. Buesching,[5,35] V. Bumazhnov,[20] G. Bunce,[5,45] J. M. Burward-Hoy,[31,32] S. Butsyk,[32,51]
X. Camard,[52] S. Campbell,[51] P. Chand,[4] B. S. Chang,[59] W. C. Chang,[2] J.-L. Charvet,[13] S. Chernichenko,[20] J. Chiba,[25]
C. Y. Chi,[11] M. Chiu,[11,21] I. J. Choi,[59] R. K. Choudhury,[4] T. Chujo,[5,56] P. Chung,[50] A. Churyn,[20] V. Cianciolo,[40] C. R. Cleven,[18]
Y. Cobigo,[13] B. A. Cole,[11] M. P. Comets,[41] P. Constantin,[23,32] M. Csanád,[15] T. Csörgő,[26] J. P. Cussonneau,[52] T. Dahms,[51]
K. Das,[17] G. David,[5] F. Deák,[15] M. B. Deaton,[1] K. Dehmelt,[16] H. Delagrange,[52] A. Denisov,[20] D. d'Enterria,[11]
A. Deshpande,[45,51] E. J. Desmond,[5] A. Devismes,[51] O. Dietzsch,[48] A. Dion,[51] M. Donadelli,[48] J. L. Drachenberg,[1] O. Drapier,[30]
A. Drees,[51] A. K. Dubey,[58] A. Durum,[20] D. Dutta,[4] V. Dzhordzhadze,[6,53] Y. V. Efremenko,[40] J. Egdemir,[51] F. Ellinghaus,[10]
W. S. Emam,[6] A. Enokizono,[31] H. En'yo,[44,45] B. Espagnon,[41] S. Esumi,[55] K. O. Eyser,[6] D. E. Fields,[38,45] C. Finck,[52]
M. Finger Jr.,[7,24] M. Finger,[7,24] F. Fleuret,[30] S. L. Fokin,[28] B. D. Fox,[45] Z. Fraenkel,[58,*] J. E. Frantz,[11,51] A. Franz,[5]
A. D. Frawley,[17] K. Fujiwara,[44] Y. Fukao,[29,44,45] S.-Y. Fung,[6] T. Fusayasu,[37] S. Gadrat,[33] I. Garishvili,[53] M. Germain,[52]
A. Glenn,[10,53] H. Gong,[51] M. Gonin,[30] J. Gosset,[13] Y. Goto,[44,45] R. Granier de Cassagnac,[30] N. Grau,[23] S. V. Greene,[56]
M. Grosse Perdekamp,[21,45] T. Gunji,[9] H.-Å. Gustafsson,[34] T. Hachiya,[19] A. Hadj Henni,[52] C. Haegemann,[38] J. S. Haggerty,[5]
H. Hamagaki,[9] R. Han,[42] A. G. Hansen,[32] H. Harada,[19] E. P. Hartouni,[31] K. Haruna,[19] M. Harvey,[5] E. Haslum,[34] K. Hasuko,[44]
R. Hayano,[9] M. Heffner,[31] T. K. Hemmick,[51] T. Hester,[6] J. M. Heuser,[44] X. He,[18] P. Hidas,[26] H. Hiejima,[21] J. C. Hill,[23]
R. Hobbs,[38] M. Hohlmann,[16] W. Holzmann,[50] K. Homma,[19] B. Hong,[27] A. Hoover,[39] T. Horaguchi,[44,45,54] D. Hornback,[53]
T. Ichihara,[44,45] V. V. Ikonnikov,[28] K. Imai,[29,44] M. Inaba,[55] Y. Inoue,[44,46] M. Inuzuka,[9] D. Isenhower,[1] L. Isenhower,[1]
M. Ishihara,[44] T. Isobe,[9] M. Issah,[50] A. Isupov,[24] B. V. Jacak,[51,†] J. Jia,[11,51] J. Jin,[11] O. Jinnouchi,[44,45] B. M. Johnson,[5]
S. C. Johnson,[31] K. S. Joo,[36] D. Jouan,[41] F. Kajihara,[9] S. Kametani,[9,57] N. Kamihara,[44,54] J. Kamin,[51] M. Kaneta,[45]
J. H. Kang,[59] H. Kanou,[44,54] K. Katou,[57] T. Kawabata,[9] D. Kawall,[45] A. V. Kazantsev,[28] S. Kelly,[10,11] B. Khachaturov,[58]
A. Khanzadeev,[43] J. Kikuchi,[57] D. H. Kim,[36] D. J. Kim,[59] E. Kim,[49] G.-B. Kim,[30] H. J. Kim,[59] E. Kinney,[10] A. Kiss,[15]
E. Kistenev,[5] A. Kiyomichi,[44] J. Klay,[31] C. Klein-Boesing,[35] H. Kobayashi,[45] L. Kochenda,[43] V. Kochetkov,[20] R. Kohara,[19]
B. Komkov,[43] M. Konno,[55] D. Kotchetkov,[6] A. Kozlov,[58] A. Král,[12] A. Kravitz,[11] P. J. Kroon,[5] J. Kubart,[7,22] C. H. Kuberg,[1,*]
G. J. Kunde,[32] N. Kurihara,[9] K. Kurita,[44,46] M. J. Kweon,[27] Y. Kwon,[53,59] G. S. Kyle,[39] R. Lacey,[50] Y.-S. Lai,[11] J. G. Lajoie,[23]
A. Lebedev,[23,28] Y. Le Bornec,[41] S. Leckey,[51] D. M. Lee,[32] M. K. Lee,[59] T. Lee,[49] M. J. Leitch,[32] M. A. L. Leite,[48] B. Lenzi,[48]
H. Lim,[49] T. Liška,[12] A. Litvinenko,[24] M. X. Liu,[32] X. Li,[8] X. H. Li,[6] B. Love,[56] D. Lynch,[5] C. F. Maguire,[56] Y. I. Makdisi,[5]
A. Malakhov,[24] M. D. Malik,[38] V. I. Manko,[28] Y. Mao,[42,44] G. Martinez,[52] L. Mašek,[7,22] H. Masui,[55] F. Matathias,[11,51]
T. Matsumoto,[9,57] M. C. McCain,[1] M. McCumber,[51] P. L. McGaughey,[32] Y. Miake,[55] P. Mikeš,[7,22] K. Miki,[55] T. E. Miller,[56]
A. Milov,[51] S. Mioduszewski,[5] G. C. Mishra,[18] M. Mishra,[3] J. T. Mitchell,[5] M. Mitrovski,[50] A. K. Mohanty,[4] A. Morreale,[6]
D. P. Morrison,[5] J. M. Moss,[32] T. V. Moukhanova,[28] D. Mukhopadhyay,[56,58] M. Muniruzzaman,[6] J. Murata,[44,46] S. Nagamiya,[25]
Y. Nagata,[55] J. L. Nagle,[10,11] M. Naglis,[58] I. Nakagawa,[44,45] Y. Nakamiya,[19] T. Nakamura,[19] K. Nakano,[44,54] J. Newby,[31,53]
M. Nguyen,[51] B. E. Norman,[32] A. S. Nyanin,[28] J. Nystrand,[34] E. O'Brien,[5] S. X. Oda,[9] C. A. Ogilvie,[23] H. Ohnishi,[44]
I. D. Ojha,[3,56] H. Okada,[29,44] K. Okada,[44,45] M. Oka,[55] O. O. Omiwade,[1] A. Oskarsson,[34] I. Otterlund,[34] M. Ouchida,[19]
K. Oyama,[9] K. Ozawa,[9] R. Pak,[5] D. Pal,[56,58] A. P. T. Palounek,[32] V. Pantuev,[51] V. Papavassiliou,[39] J. Park,[49] W. J. Park,[27]
S. F. Pate,[39] H. Pei,[23] V. Penev,[24] J.-C. Peng,[21] H. Pereira,[13] V. Peresedov,[24] D. Yu. Peressounko,[28] A. Pierson,[38]
C. Pinkenburg,[5] R. P. Pisani,[5] M. L. Purschke,[5] A. K. Purwar,[32,51] J. M. Qualls,[1] H. Qu,[18] J. Rak,[23,38] A. Rakotozafindrabe,[30]
I. Ravinovich,[58] K. F. Read,[40,53] S. Rembeczki,[16] M. Reuter,[51] K. Reygers,[35] V. Riabov,[43] Y. Riabov,[43] G. Roche,[33]
A. Romana,[30,*] M. Rosati,[23] S. S. E. Rosendahl,[34] P. Rosnet,[33] P. Rukoyatkin,[24] V. L. Rykov,[44] S. S. Ryu,[59] B. Sahlmueller,[35]
N. Saito,[29,44,45] T. Sakaguchi,[5,9,57] S. Sakai,[55] H. Sakata,[19] V. Samsonov,[43] L. Sanfratello,[38] R. Santo,[35] H. D. Sato,[29,44]
S. Sato,[5,25,55] S. Sawada,[25] Y. Schutz,[52] J. Seele,[10] R. Seidl,[21] V. Semenov,[20] R. Seto,[6] D. Sharma,[58] T. K. Shea,[5] I. Shein,[20]
A. Shevel,[43,50] T.-A. Shibata,[44,54] K. Shigaki,[19] M. Shimomura,[55] K. Shoji,[29,44] A. Sickles,[51] C. L. Silva,[48] D. Silvermyr,[32,40]
C. Silvestre,[13] K. S. Sim,[27] C. P. Singh,[3] V. Singh,[3] S. Skutnik,[23] M. Slunečka,[7,24] A. Soldatov,[20] R. A. Soltz,[31]
W. E. Sondheim,[32] S. P. Sorensen,[53] I. V. Sourikova,[5] F. Staley,[13] P. W. Stankus,[40] E. Stenlund,[34] M. Stepanov,[39] A. Ster,[26]
S. P. Stoll,[5] T. Sugitate,[19] C. Suire,[41] J. P. Sullivan,[32] J. Sziklai,[26] T. Tabaru,[45] S. Takagi,[55] E. M. Takagui,[48] A. Taketani,[44,45]
K. H. Tanaka,[25] Y. Tanaka,[37] K. Tanida,[44,45] M. J. Tannenbaum,[5] A. Taranenko,[50] P. Tarján,[14] T. L. Thomas,[38] M. Togawa,[29,44]
A. Toia,[51] J. Tojo,[44] L. Tomášek,[22] H. Torii,[29,44,45] R. S. Towell,[1] V.-N. Tram,[30] I. Tserruya,[58] Y. Tsuchimoto,[19] H. Tydesjö,[34]
N. Tyurin,[20] T. J. Uam,[36] C. Vale,[23] H. Valle,[56] H. W. van Hecke,[32] J. Velkovska,[5,56] M. Velkovsky,[51] R. Vertesi,[14]
V. Veszprémi,[14] A. A. Vinogradov,[28] M. Virius,[12] M. A. Volkov,[28] V. Vrba,[22] E. Vznuzdaev,[43] M. Wagner,[29,44] D. Walker,[51]
X. R. Wang,[18,39] Y. Watanabe,[44,45] J. Wessels,[35] S. N. White,[5] N. Willis,[41] D. Winter,[11] F. K. Wohn,[23] C. L. Woody,[5]

0556-2813/2008/77(2)/024912(15)

M. Wysocki,[10] W. Xie,[6,45] Y. L. Yamaguchi,[57] A. Yanovich,[20] Z. Yasin,[6] J. Ying,[18] S. Yokkaichi,[44,45] G. R. Young,[40] I. Younus,[38] I. E. Yushmanov,[28] W. A. Zajc,[11] O. Zaudtke,[35] C. Zhang,[11,40] S. Zhou,[8] J. Zimányi,[26,*] L. Zolin,[24] and X. Zong[23]
(PHENIX Collaboration)

[1]*Abilene Christian University, Abilene, Texas 79699, USA*
[2]*Institute of Physics, Academia Sinica, Taipei 11529, Taiwan*
[3]*Department of Physics, Banaras Hindu University, Varanasi 221 005, India*
[4]*Bhabha Atomic Research Centre, Bombay 400 085, India*
[5]*Brookhaven National Laboratory, Upton, New York 11973-5000, USA*
[6]*University of California—Riverside, Riverside, California 92521, USA*
[7]*Charles University, Ovocný trh 5, Praha 1, CZ-116 36 Prague, Czech Republic*
[8]*China Institute of Atomic Energy (CIAE), Beijing, People's Republic of China*
[9]*Center for Nuclear Study, Graduate School of Science, University of Tokyo, 7-3-1 Hongo, Bunkyo, Tokyo 113-0033, Japan*
[10]*University of Colorado, Boulder, Colorado 80309, USA*
[11]*Columbia University, New York 10027, and Nevis Laboratories, Irvington, New York 10533, USA*
[12]*Czech Technical University, Zikova 4, CZ-166 36 Prague 6, Czech Republic*
[13]*Dapnia, CEA Saclay, F-91191 Gif-sur-Yvette, France*
[14]*Debrecen University, Egyetem tér 1, H-4010 Debrecen, Hungary*
[15]*ELTE, Eötvös Loránd University, Pázmány P. s. 1/A, H-1117 Budapest, Hungary*
[16]*Florida Institute of Technology, Melbourne, Florida 32901, USA*
[17]*Florida State University, Tallahassee, Florida 32306, USA*
[18]*Georgia State University, Atlanta, Georgia 30303, USA*
[19]*Hiroshima University, Kagamiyama, Higashi-Hiroshima 739-8526, Japan*
[20]*IHEP Protvino, State Research Center of Russian Federation, Institute for High Energy Physics, Protvino, RU-142281, Russia*
[21]*University of Illinois at Urbana-Champaign, Urbana, Illinois 61801, USA*
[22]*Institute of Physics, Academy of Sciences of the Czech Republic, Na Slovance 2, CZ-182 21 Prague 8, Czech Republic*
[23]*Iowa State University, Ames, Iowa 50011, USA*
[24]*Joint Institute for Nuclear Research, RU-141980 Dubna, Moscow Region, Russia*
[25]*KEK, High Energy Accelerator Research Organization, Tsukuba, Ibaraki 305-0801, Japan*
[26]*KFKI Research Institute for Particle and Nuclear Physics of the Hungarian Academy of Sciences (MTA KFKI RMKI), Post Office Box 49, H-1525 Budapest 114, Hungary*
[27]*Korea University, Seoul, 136-701, Korea*
[28]*Russian Research Center "Kurchatov Institute," Moscow, Russia*
[29]*Kyoto University, Kyoto 606-8502, Japan*
[30]*Laboratoire Leprince-Ringuet, Ecole Polytechnique, CNRS-IN2P3, Route de Saclay, F-91128 Palaiseau, France*
[31]*Lawrence Livermore National Laboratory, Livermore, California 94550, USA*
[32]*Los Alamos National Laboratory, Los Alamos, New Mexico 87545, USA*
[33]*LPC, Université Blaise Pascal, CNRS-IN2P3, Clermont-Fd, F-63177 Aubiere Cedex, France*
[34]*Department of Physics, Lund University, Box 118, SE-221 00 Lund, Sweden*
[35]*Institut für Kernphysik, University of Muenster, D-48149 Muenster, Germany*
[36]*Myongji University, Yongin, Kyonggido 449-728, Korea*
[37]*Nagasaki Institute of Applied Science, Nagasaki-shi, Nagasaki 851-0193, Japan*
[38]*University of New Mexico, Albuquerque, New Mexico 87131, USA*
[39]*New Mexico State University, Las Cruces, New Mexico 88003, USA*
[40]*Oak Ridge National Laboratory, Oak Ridge, Tennessee 37831, USA*
[41]*IPN-Orsay, Universite Paris Sud, CNRS-IN2P3, BP1, F-91406 Orsay, France*
[42]*Peking University, Beijing, People's Republic of China*
[43]*PNPI, Petersburg Nuclear Physics Institute, Gatchina, Leningrad Region, RU-188300, Russia*
[44]*RIKEN, The Institute of Physical and Chemical Research, Wako, Saitama 351-0198, Japan*
[45]*RIKEN BNL Research Center, Brookhaven National Laboratory, Upton, New York 11973-5000, USA*
[46]*Physics Department, Rikkyo University, 3-34-1 Nishi-Ikebukuro, Toshima, Tokyo 171-8501, Japan*
[47]*Saint Petersburg State Polytechnic University, St. Petersburg, Russia*
[48]*Universidade de São Paulo, Instituto de Física, Caixa Postal 66318, São Paulo CEP05315-970, Brazil*
[49]*System Electronics Laboratory, Seoul National University, Seoul, Korea*
[50]*Chemistry Department, Stony Brook University, Stony Brook, SUNY, New York 11794-3400, USA*
[51]*Department of Physics and Astronomy, Stony Brook University, SUNY, Stony Brook, New York 11794, USA*
[52]*SUBATECH (Ecole des Mines de Nantes, CNRS-IN2P3, Université de Nantes) BP 20722, F-44307, Nantes, France*
[53]*University of Tennessee, Knoxville, Tennessee 37996, USA*
[54]*Department of Physics, Tokyo Institute of Technology, Oh-okayama, Meguro, Tokyo 152-8551, Japan*

[55]Institute of Physics, University of Tsukuba, Tsukuba, Ibaraki 305, Japan
[56]Vanderbilt University, Nashville, Tennessee 37235, USA
[57]Waseda University, Advanced Research Institute for Science and Engineering, 17 Kikui-cho, Shinjuku-ku, Tokyo 162-0044, Japan
[58]Weizmann Institute, Rehovot 76100, Israel
[59]Yonsei University, IPAP, Seoul 120-749, Korea

(Received 26 November 2007; published 28 February 2008)

We present a new analysis of J/ψ production yields in deuteron-gold collisions at $\sqrt{s_{NN}} = 200$ GeV using data taken from the PHENIX experiment in 2003 and previously published in S. S. Adler *et al.* [Phys. Rev. Lett **96**, 012304 (2006)]. The high statistics proton-proton J/ψ data taken in 2005 are used to improve the baseline measurement and thus construct updated cold nuclear matter modification factors ($R_{d\mathrm{Au}}$). A suppression of J/ψ in cold nuclear matter is observed as one goes forward in rapidity (in the deuteron-going direction), corresponding to a region more sensitive to initial-state low-x gluons in the gold nucleus. The measured nuclear modification factors are compared to theoretical calculations of nuclear shadowing to which a J/ψ (or precursor) breakup cross section is added. Breakup cross sections of $\sigma_{\mathrm{breakup}} = 2.8^{+1.7}_{-1.4}$ $(2.2^{+1.6}_{-1.5})$ mb are obtained by fitting these calculations to the data using two different models of nuclear shadowing. These breakup cross-section values are consistent within large uncertainties with the 4.2 ± 0.5 mb determined at lower collision energies. Projecting this range of cold nuclear matter effects to copper-copper and gold-gold collisions reveals that the current constraints are not sufficient to firmly quantify the additional hot nuclear matter effect.

DOI: 10.1103/PhysRevC.77.024912 PACS number(s): 25.75.Dw

I. INTRODUCTION

Understanding the behavior of QCD matter under different conditions of temperature and density is the subject of intense experimental and theoretical work in nuclear physics. The transition from hadronic matter to a quark-gluon plasma at high temperature is expected to be achieved in high-energy heavy-ion collisions. The hadronization of partons in vacuum or cold nuclear matter (i.e., in a nucleus) is also of keen interest and represents a nonperturbative and dynamic QCD process. The formation and interaction of heavy quarkonia (e.g., J/ψ mesons) in vacuum, cold nuclear matter, and hot nuclear matter present an excellent laboratory for gaining insights on these transformations. Recent results from the Relativistic Heavy Ion Collider reveal a significant suppression of the final J/ψ yield in central (small impact parameter) Au + Au reactions at $\sqrt{s_{NN}} = 200$ GeV, relative to expectations scaled from $p + p$ reactions at the same energy [1,2]. A possible source of this suppression is the screening of the attractive interaction between the quark-antiquark pair in the hot nuclear medium, as temperatures are expected to be above the critical temperature for a quark-gluon plasma transition. Larger J/ψ suppression is observed at forward rapidity than at midrapidity, which contradicts models with only color screening of quarkonia proportional to the local energy density.

Produced $c\bar{c}$ pairs must pass through the remaining nuclear material from the incident cold nuclei, in addition to surviving any hot medium environment. The so-called cold nuclear matter effects [3], including modification of initial parton distribution functions (shadowing, gluon saturation, antishadowing, EMC effect, etc.), initial- and final-state partonic multiple scattering, and related initial-state parton energy loss need to be accounted for before firm conclusions can be drawn about the effect of the hot medium thought to be created. In fact, these various cold nuclear matter effects are interesting in their own right, notably in terms of hadronization time scales, parton energy loss in matter, and the various initial-state effects just mentioned.

This paper presents a new analysis of the modification of J/ψ production in deuteron-gold (d + Au) collisions relative to proton-proton ($p + p$) collisions at $\sqrt{s_{NN}} = 200$ GeV and the implications for understanding the Au + Au and Cu + Cu data at the same energy. The PHENIX experiment has previously published a result using $p + p$ and d + Au data taken in 2003 [4]. A modest J/ψ suppression was observed at forward rapidity (i.e., in the deuteron-moving direction), which is a possible indication of shadowing of low-x gluons in the gold nucleus. A substantially larger (more than an order of magnitude) $p + p$ data set was recorded in 2005, with the J/ψ results published in Ref. [2], and has been used as the baseline for recent Au + Au and Cu + Cu nuclear modification factors [1,5]. The same $p + p$ data set is used in the analysis presented here to determine the d + Au nuclear modifications more accurately and in a fully consistent way with those in the Au + Au and Cu + Cu cases. In addition, during the two years between the analyses of the 2003 and 2005 data sets significant improvements in the reconstruction software and signal-extraction method were achieved along with an overall better understanding of the detector performance. These improvements have been included in this analysis, allowing maximal cancellation of systematic errors when using the 2005 $p + p$ data sample to form the J/ψ nuclear modification factor. We first describe the updated analysis, then present the new nuclear modification factors and their implications.

II. EXPERIMENT

The PHENIX apparatus is described in Ref. [6]. It consists of two sets of spectrometers referred to as the central arms,

---

[*] Deceased.

[†] PHENIX Spokesperson; electronic address: jacak@skipper.physics.sunysb.edu

which measure particles emitted at midrapidity ($|y| < 0.35$), and the muon arms, measuring particles emitted at backward and forward rapidity ($-2.2 < y < -1.2$ and $1.2 < y < 2.2$).

At midrapidity, J/ψ particles are measured via their decay into two electrons. Electrons are identified by matching tracks reconstructed with drift chambers (DC) and pad chambers (PC) to clusters in the electromagnetic calorimeters (EMCAL) and hits in the ring imaging Cerenkov counters (RICH). In $d + \mathrm{Au}$ collisions, a charged track is identified as an electron candidate by requiring at least three matching RICH phototube hits within a certain radius with respect to the the center defined by the track projection at the RICH, a position matching of ±4 standard deviations between the EMCAL cluster and the reconstructed track, and a cut on the ratio of energy to momentum. In $p + p$ collisions the electron identification cuts are the same except that only two matching RICH phototube hits are required.

At forward and backward rapidity, J/ψ particles are measured via their decay into two muons. Muons are identified by matching tracks measured in cathode strip chambers (referred to as the muon tracker, or MuTR) to hits in alternating planes of Iarocci tubes and steel absorbers (referred to as the muon identifier, or MuID). Each muon arm is located behind a thick copper and iron absorber that is meant to absorb most hadrons produced during the collisions, so that the measured muons must penetrate 8 to 11 interaction lengths of material in total.

The $d + \mathrm{Au}$ data used for this analysis were recorded in 2003 using a minimum-bias trigger that required hits in each of the two beam-beam counters (BBCs) located at positive and negative rapidity ($3 < |\eta| < 3.9$) and represent integrated luminosities for the different spectrometers ranging from 1.4 to 1.7 nb^{-1} (or, equivalently, from 2.7 to 3.4 billion interactions). This trigger covers $88\% \pm 4\%$ of the total $d + \mathrm{Au}$ inelastic cross section of 2260 mb [7]. For the electrons, an additional trigger was used that required one hit above threshold in the EMCAL and a matching hit in the RICH. For the muons, two additional triggers were used at different times during the data-taking period. The muon triggers are based on information from the MuID, which has five active detector layers between the steel absorbers. For the first part of the data-taking period, one of the tracks was required to reach the fourth MuID plane, while the other was only required to reach the second MuID plane. For the latter part, the trigger required at least two tracks to reach the fourth MuID plane of Iarocci tubes.

The BBCs are also used to determine the centrality of the $d + \mathrm{Au}$ collisions by measuring the energy deposited in the counters located at negative rapidity (in the gold-going direction). For a given centrality bin, the average number of equivalent nucleon-nucleon collisions (N_{coll}) is derived from this energy by using a Glauber calculation [8] coupled to a simulation of the BBC. The centrality bins used in this analysis and the corresponding number of collisions are listed in Table I. To ensure that the centrality categories are well defined, collisions are required to be within ±30 cm of the center of the interaction region.

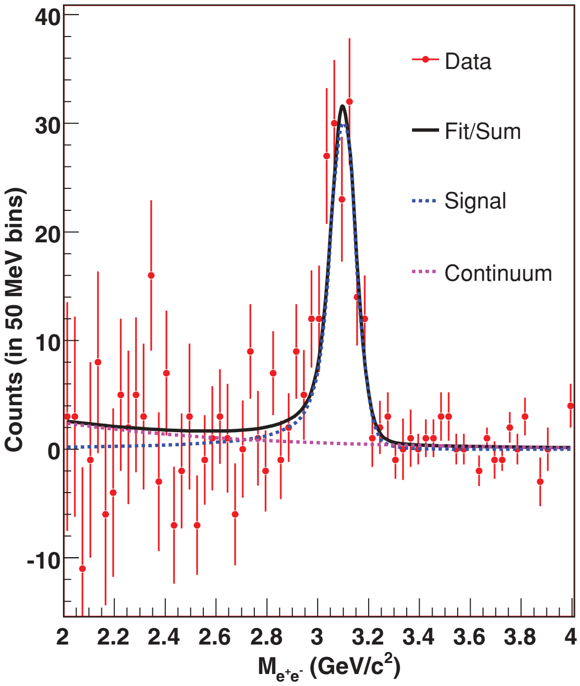

FIG. 1. (Color online) Invariant mass spectra in minimum-bias $d + \mathrm{Au}$ reactions for $J/\psi \longrightarrow e^+e^-$ at $|y| < 0.35$, with the functional forms used to extract the number of reconstructed J/ψ mesons.

III. SIGNAL EXTRACTION

The number of J/ψ particles is determined by using the invariant mass distribution of unlike-sign lepton pairs. At midrapidity, the J/ψ signal count is obtained via counting the number of unlike-sign dielectrons after subtracting the like-sign pairs in a fixed mass window of $2.6 \leqslant M_{e^+e^-} \leqslant 3.6\ \mathrm{GeV}/c^2$ or $2.7 \leqslant M_{e^+e^-} \leqslant 3.5\ \mathrm{GeV}/c^2$, depending on the number of DC hits required for track reconstruction. Figure 1 shows the J/ψ mass spectrum after subtracting the background. The solid

TABLE I. Characterization of the collision centrality for $d + \mathrm{Au}$ collisions. Listed are the centrality bins used in this analysis, the corresponding number of binary collisions, N_{coll}, and the values of $c = \epsilon^{\mathrm{BBC}}_{\mathrm{MB(cent)}}/\epsilon^{\mathrm{BBC}}_{J/\psi}$ for J/ψ mesons emitted in the three rapidity ranges used for this analysis.

Centrality	0–20%	20–40%	40–60%	60–88%	0–100%
N_{coll}	15.4 ± 1.0	10.6 ± 0.7	7.0 ± 0.6	3.1 ± 0.3	7.6 ± 0.3
c ($\lvert y \rvert < 0.35$)	0.95 ± 0.03	0.99 ± 0.01	1.03 ± 0.01	1.04 ± 0.03	0.94 ± 0.02
c ($-2.2 < y < -1.2$)	0.93 ± 0.03	0.99 ± 0.01	1.04 ± 0.01	1.05 ± 0.03	0.94 ± 0.02
c ($1.2 < y < 2.2$)	1.00 ± 0.03	1.00 ± 0.01	1.02 ± 0.01	1.02 ± 0.03	0.94 ± 0.02

black line is the sum of the J/ψ line shape (dashed curve) and an exponential function (dot-dashed curve) describing the continuum component determined from the 2005 $p+p$ data set [2]. The J/ψ line-shape function takes into account the momentum resolution of track reconstruction, internal radiative effects [9], and external radiative effects evaluated by using a GEANT [10] simulation of the PHENIX detector. The number of J/ψ particles in $d+$ Au collisions is too small to allow a good fit but a comparison between $d+$ Au and $p+p$ J/ψ line shapes shows good agreement. The fraction of J/ψ candidates outside of the mass window owing to the radiative effects is estimated to be 7.2% ± 1.0% based on the line-shape functions. The J/ψ signal is also corrected for the dielectron continuum yield, which originates primarily from open charm and Drell-Yan pairs inside the mass window. The estimated contribution is 10% ± 5%, based on the fitting function and PYTHIA [11] simulations. Approximately 400 J/ψ mesons are obtained.

At backward and forward rapidity an event-mixing technique is now used to estimate the combinatorial background, whereas the like-sign pairs were used in the previous analysis [4]. The previous method suffered from a larger statistical uncertainty for bins where the signal over background is poor. A sample mass distribution after the subtraction of the mixed-event background is shown in Fig. 2. Approximately 500 and 750 J/ψ mesons are obtained for backward and forward rapidity, respectively. The signal counts are determined from this subtracted dimuon invariant mass distribution with a log-likelihood fit and for three different assumed functional forms and parameters. In all three cases, an exponential form is used to account for correlated physical background sources (e.g., Drell-Yan or open charm) and the possible systematic offset in the normalization of the mixed-event background. The number of J/ψ particles is then estimated by direct counting of the remaining number of pairs above the exponential in the mass range $2.6 \leqslant M_{\mu^+\mu^-} \leqslant 3.6$ GeV/c^2, using a Gaussian function with the center fixed to the J/ψ mass and the width and integrated yield left free, or using two Gaussian functions for which both the center and widths are fixed to the values measured in $p+p$ collisions. The two Gaussian functions account for the non-Gaussian tails in the invariant mass distribution. The normalization of the mixed background is varied by a systematic uncertainty of ±2% prior to its subtraction from the mass distribution. This uncertainty is determined by comparing different normalization methods. The corresponding signal variations are included in the systematic uncertainty. Because of the particular fit procedure, for all $p+p$ and $d+$ Au cases this normalization uncertainty results in a very small systematic uncertainty on the number of measured J/ψ particles. This entire procedure is identical to the one used in Refs. [1,2].

IV. INVARIANT YIELD

The J/ψ invariant yield in a given centrality, transverse momentum, and rapidity bin is

$$\frac{B_{ll}}{2\pi p_{\rm T}}\frac{d^2N_{J/\psi}}{dp_T\,dy} = \frac{1}{2\pi p_T\,\Delta p_T\,\Delta y}\,\frac{N^{J/\psi}_{\rm counts}}{A\epsilon_{\rm rec}\epsilon_{\rm trig}N^{\rm MB}_{\rm evt}}\,\frac{\epsilon^{\rm BBC}_{\rm MB(cent)}}{\epsilon^{\rm BBC}_{J/\psi}}, \qquad (1)$$

where B_{ll} is the branching ratio for $J/\psi \to l^+l^-$, $N^{J/\psi}_{\rm counts}$ is the number of reconstructed J/ψ mesons, $N^{\rm MB}_{\rm evt}$ is the number of minimum-bias events sampled, $\epsilon^{\rm BBC}_{\rm MB(cent)}$ is the BBC trigger efficiency for minimum-bias events in a given centrality

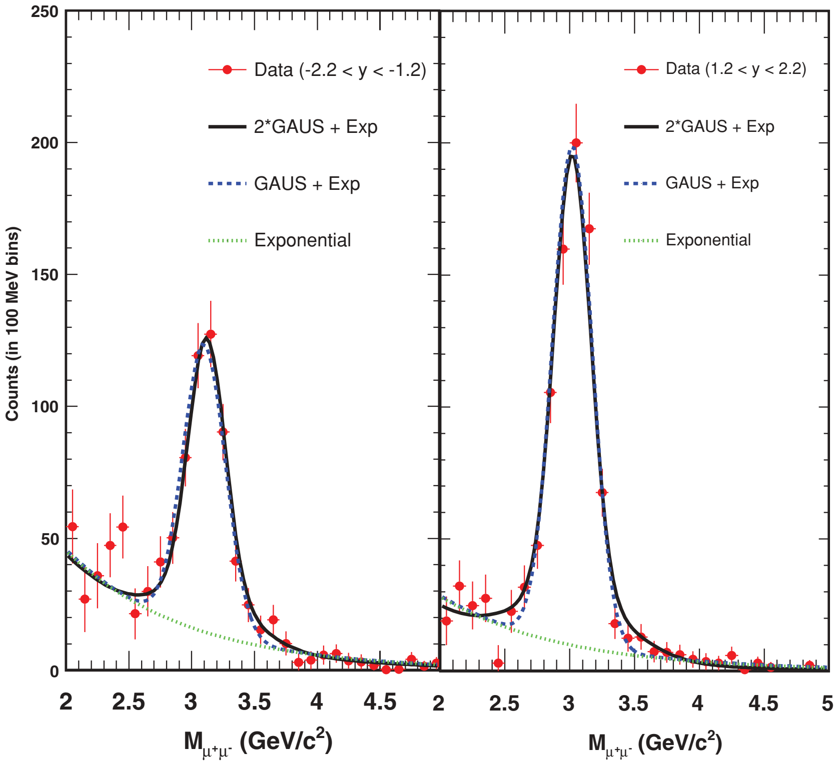

FIG. 2. (Color online) Invariant mass spectra in minimum-bias $d+$ Au reactions for (left) $J/\psi \longrightarrow \mu^+\mu^-$ at $-2.2 < y < -1.2$ and (right) $J/\psi \longrightarrow \mu^+\mu^-$ at $1.2 < y < 2.2$, with the functional forms used to extract the number of reconstructed J/ψ mesons.

TABLE II. Statistical and type A systematic uncertainties added in quadrature and type B systematic uncertainties. Type C errors are shown in the relevant figures.

Rapidity	Centrality (%)	p_T (GeV/c)	y	Invariant yield	$R_{d\mathrm{Au}}$
Backward rapidity results	0–100	All	$[-2.2, -1.2]$	$(4.264 \pm 0.326 \pm 0.923) \times 10^{-6}$	$0.90 \pm 0.08 \pm 0.19$
	0–100	All	$[-2.2, -1.7]$	$(3.583 \pm 0.395 \pm 0.775) \times 10^{-6}$	$0.95 \pm 0.12 \pm 0.20$
	0–100	All	$[-1.7, -1.2]$	$(5.292 \pm 0.483 \pm 1.145) \times 10^{-6}$	$0.90 \pm 0.09 \pm 0.19$
	0–100	0–1	$[-2.2, -1.2]$	$(3.040 \pm 0.460 \pm 0.658) \times 10^{-7}$	$0.69 \pm 0.11 \pm 0.15$
	0–100	1–2	$[-2.2, -1.2]$	$(1.782 \pm 0.201 \pm 0.386) \times 10^{-7}$	$0.84 \pm 0.10 \pm 0.18$
	0–100	2–3	$[-2.2, -1.2]$	$(8.141 \pm 0.937 \pm 1.762) \times 10^{-8}$	$1.44 \pm 0.18 \pm 0.31$
	0–100	3–4	$[-2.2, -1.2]$	$(1.789 \pm 0.359 \pm 0.387) \times 10^{-8}$	$1.21 \pm 0.26 \pm 0.26$
	0–100	4–5	$[-2.2, -1.2]$	$(4.016 \pm 1.451 \pm 0.869) \times 10^{-9}$	$1.14 \pm 0.43 \pm 0.24$
	0–20	All	$[-2.2, -1.2]$	$(9.084 \pm 0.922 \pm 1.925) \times 10^{-6}$	$0.94 \pm 0.10 \pm 0.21$
	20–40	All	$[-2.2, -1.2]$	$(3.676 \pm 0.642 \pm 0.770) \times 10^{-6}$	$0.55 \pm 0.10 \pm 0.12$
	40–60	All	$[-2.2, -1.2]$	$(4.013 \pm 0.583 \pm 0.842) \times 10^{-6}$	$0.92 \pm 0.14 \pm 0.21$
	60–88	All	$[-2.2, -1.2]$	$(2.062 \pm 0.312 \pm 0.436) \times 10^{-6}$	$1.07 \pm 0.17 \pm 0.25$
Midrapidity results	0–100	All	$[-0.35, 0.35]$	$(6.750 \pm 0.540 \pm 0.950) \times 10^{-6}$	$0.85 \pm 0.07 \pm 0.15$
	0–100	0–1	$[-0.35, 0.35]$	$(6.700 \pm 0.800 \pm 0.940) \times 10^{-7}$	$1.05 \pm 0.14 \pm 0.21$
	0–100	1–2	$[-0.35, 0.35]$	$(2.400 \pm 0.340 \pm 0.340) \times 10^{-7}$	$0.74 \pm 0.11 \pm 0.15$
	0–100	2–3	$[-0.35, 0.35]$	$(1.200 \pm 0.190 \pm 0.170) \times 10^{-7}$	$0.96 \pm 0.17 \pm 0.19$
	0–100	3–4	$[-0.35, 0.35]$	1.37×10^{-8} (90% CL)	0.41 (90% CL)
	0–100	4–5	$[-0.35, 0.35]$	$(7.500 \pm 3.600 \pm 1.100) \times 10^{-9}$	$1.09 \pm 0.61 \pm 0.22$
	0–20	All	$[-0.35, 0.35]$	$(1.144 \pm 0.160 \pm 0.160) \times 10^{-5}$	$0.71 \pm 0.10 \pm 0.12$
	20–40	All	$[-0.35, 0.35]$	$(7.990 \pm 1.290 \pm 1.120) \times 10^{-6}$	$0.71 \pm 0.12 \pm 0.11$
	40–60	All	$[-0.35, 0.35]$	$(6.800 \pm 1.010 \pm 0.950) \times 10^{-6}$	$0.93 \pm 0.14 \pm 0.14$
	60–88	All	$[-0.35, 0.35]$	$(3.030 \pm 0.500 \pm 0.420) \times 10^{-6}$	$0.94 \pm 0.16 \pm 0.14$
Forward rapidity results	0–100	All	$[1.2, 2.2]$	$(3.300 \pm 0.242 \pm 0.592) \times 10^{-6}$	$0.63 \pm 0.06 \pm 0.11$
	0–100	All	$[1.2, 1.7]$	$(4.522 \pm 0.341 \pm 0.811) \times 10^{-6}$	$0.68 \pm 0.06 \pm 0.11$
	0–100	All	$[1.7, 2.2]$	$(2.406 \pm 0.224 \pm 0.432) \times 10^{-6}$	$0.59 \pm 0.06 \pm 0.10$
	0–100	0–1	$[1.2, 2.2]$	$(2.779 \pm 0.285 \pm 0.498) \times 10^{-7}$	$0.55 \pm 0.06 \pm 0.09$
	0–100	1–2	$[1.2, 2.2]$	$(1.362 \pm 0.115 \pm 0.244) \times 10^{-7}$	$0.60 \pm 0.06 \pm 0.10$
	0–100	2–3	$[1.2, 2.2]$	$(4.667 \pm 0.566 \pm 0.837) \times 10^{-8}$	$0.73 \pm 0.10 \pm 0.12$
	0–100	3–4	$[1.2, 2.2]$	$(1.472 \pm 0.225 \pm 0.264) \times 10^{-8}$	$0.93 \pm 0.16 \pm 0.16$
	0–100	4–5	$[1.2, 2.2]$	$(2.842 \pm 0.756 \pm 0.510) \times 10^{-9}$	$0.84 \pm 0.25 \pm 0.14$
	0–20	All	$[1.2, 2.2]$	$(5.705 \pm 0.501 \pm 0.987) \times 10^{-6}$	$0.54 \pm 0.05 \pm 0.09$
	20–40	All	$[1.2, 2.2]$	$(4.577 \pm 0.474 \pm 0.783) \times 10^{-6}$	$0.62 \pm 0.07 \pm 0.11$
	40–60	All	$[1.2, 2.2]$	$(2.950 \pm 0.347 \pm 0.505) \times 10^{-6}$	$0.62 \pm 0.08 \pm 0.11$
	60–88	All	$[1.2, 2.2]$	$(1.671 \pm 0.195 \pm 0.289) \times 10^{-6}$	$0.79 \pm 0.10 \pm 0.15$

category, Δp_T and Δy are the p_T and y bin widths, A and ϵ_{rec} are the acceptance and reconstruction efficiency corrections, ϵ_{trig} is the additional J/ψ trigger efficiency, and $\epsilon^{\mathrm{BBC}}_{J/\psi}$ is the BBC efficiency for events containing a J/ψ. All invariant yields as a function of p_T and y including statistical and systematic uncertainties are given in Table II.

The experiment measures the number of J/ψ particles per BBC triggered events, which in $d+\mathrm{Au}$ collisions represent only $88\% \pm 4\%$ of the total inelastic cross section. An additional correction is then applied such that the invariant yield represents 100% of the total inelastic cross section (as done in previous PHENIX $d+\mathrm{Au}$ analyses). The correction factor ratio $\epsilon^{\mathrm{BBC}}_{\mathrm{MB(cent)}}/\epsilon^{\mathrm{BBC}}_{J/\psi}$ depends *a priori* on the centrality bin and the rapidity range of the measured J/ψ particles. The values are given in Table I. The same procedure is applied for $p+p$ collisions, so that the yields are normalized to the $p+p$ total inelastic cross section of 42 mb.

The acceptance and efficiency corrections are determined by using a full GEANT simulation [10] of the detector with realistic resolutions and detector plane efficiencies determined from real data. Compared to the original result [4], this simulation benefits from improvements in the understanding of the detector alignment, resolution, and overall performance. It also includes the improvements added to the reconstruction software and used for the recent $p+p$, $\mathrm{Cu}+\mathrm{Cu}$, and

TABLE III. Sources of systematic uncertainties on the J/ψ invariant yield in $d+\mathrm{Au}$ collisions. Columns 2 (3) are the average values at midrapidity (forward rapidity). When two values are given, the first (second) is for peripheral (central) collisions. Uncertainties of type A (type B) are point-to-point uncorrelated (correlated).

Source	$\lvert y\rvert < 0.35$	$\lvert y\rvert \in [1.2, 2.2]$	Type
signal extraction	6%	<10%	A
acceptance	8%	10%	B
efficiency	6%	8–20%	B
run-by-run variation	5%	8%	B
input y, p_T distributions	2%	4%	B
embedding	4%	5%	B

Au + Au analyses [1,2,5]. Although the additional underlying hit occupancies per event are modest in $p+p$ and $d+\mathrm{Au}$ collisions, they are accounted for by embedding the simulated J/ψ mesons in real data events. The observed differences (4–5%) between embedded and nonembedded events are not significant given the statistics of the simulations, and therefore they are included only as a contribution to the systematic uncertainty.

The systematic uncertainties in the J/ψ invariant yield (Table III) are grouped into three categories as in the previous analyses: point-to-point uncorrelated (type A), for which the points can move independently from one another; point-to-point correlated (type B), for which the points can move coherently though not necessarily by the same amount; and global uncertainties (type C), for which all points move by the same multiplicative factor. Statistical and uncorrelated systematic uncertainties (type A) are summed in quadrature and represented as vertical bars. Type B uncertainties are represented with boxes. Type C globally correlated systematic uncertainties are quoted directly on the figures.

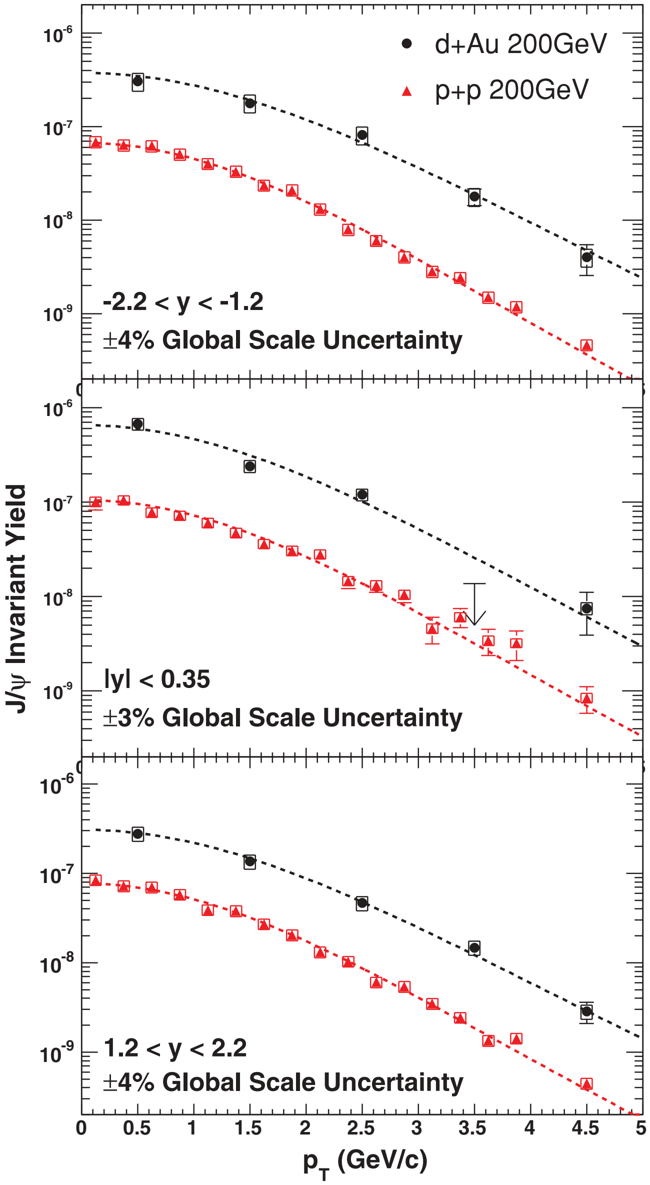

FIG. 3. (Color online) J/ψ invariant yield versus p_T in $d+\mathrm{Au}$ collisions and $p+p$ collisions. The three panels are for rapidity selections $-2.2 < y < -1.2$, $|y| < 0.35$, and $1.2 < y < 2.2$ from top to bottom. See text for description of the uncertainties and details of the functional fits.

TABLE IV. $\langle p_T^2\rangle$ calculated from a fit to the data and restricted to the range $0 < p_T < 5$ GeV/c. See text for description of the uncertainties.

Species	Rapidity	$\langle p_T^2\rangle[0, 5]$
$d+\mathrm{Au}$	$[-2.2, -1.2]$	$4.3 \pm 0.3 \pm 0.4$
$d+\mathrm{Au}$	$[-0.35, 0.35]$	$3.9 \pm 0.3 \pm 0.3$
$d+\mathrm{Au}$	$[1.2, 2.2]$	$4.0 \pm 0.2 \pm 0.4$
$p+p$	$[-2.2, -1.2]$	$3.4 \pm 0.1 \pm 0.1$
$p+p$	$[-0.35, 0.35]$	$4.1 \pm 0.2 \pm 0.1$
$p+p$	$[1.2, 2.2]$	$3.4 \pm 0.1 \pm 0.1$

Figure 3 shows the invariant J/ψ yield as a function of transverse momentum for $d+\mathrm{Au}$ collisions from this new analysis together with the published invariant yield measured in $p+p$ collisions [2]. From these yields, a $\langle p_T^2\rangle$ is calculated by using the following generic functional form to fit the data:

$$\frac{d^2N}{p_T\,dp_T} \sim A[1+(p_T/B)^2]^{-6}. \tag{2}$$

To account for finite p_T binning, the fit function is first integrated over each Δp_T range and the integral is compared to data in the corresponding bin. The measured $\langle p_T^2\rangle$ values as well as the associated statistical and systematic uncertainties are shown in Table IV.

In previous J/ψ analyses [1,2], it was found that only for the high-statistics $p+p$ data set (where the measurement has good precision out to $p_T \approx 8$ GeV/c) is the functional form of the p_T spectrum well constrained. In the Au + Au case, the functional form is not well constrained and leads to a very large systematic uncertainty on $\langle p_{\mathrm{T}}^2 \rangle$ if integrated from 0 to ∞. The integral was therefore limited to $p_{\mathrm{T}} < 5$ GeV/c, where it is best constrained by the data. The d + Au data set suffers from the same statistical limitations and the same truncation to $p_{\mathrm{T}} < 5$ GeV/c is applied. Finally, this constraint is also applied to the $p + p$ case to make a direct comparison possible.

Two uncertainties are quoted in Table IV. The first corresponds to the statistical and point-to-point uncorrelated systematic uncertainties (type A) on the measured yields. It is obtained directly from the fit by using the second derivatives of the χ^2 surface at the minimum. The second corresponds to the point-to-point correlated systematic uncertainties (type B). The contribution from type B uncertainty is estimated independently by coherently moving the measured points within the one-standard-deviation limit given by these uncertainties, allowing them to be either correlated or anticorrelated, and then redoing the fit in all cases. The largest difference observed in the values obtained by the fit is used as an upper limit to the one-standard-deviation point-to-point correlated uncertainties on $\langle p_{\mathrm{T}}^2 \rangle$.

In our previous publication [4] values for the fully integrated $\langle p_{\mathrm{T}}^2 \rangle$ in $p + p$ and d + Au collisions are quoted. However, a significant systematic uncertainty originating from not knowing the functional form to best describe the data was found that was not included in the uncertainty quoted in the paper. In addition, the new analysis revealed a bias in the previous result that increased the signal, particularly in the lowest p_{T} bin. This bias is now corrected by using the mixed-event background-subtraction technique described here together with the modified log-likelihood fit over a more appropriate range, corresponding to the region where the physical background can accurately be described by a single exponential function. Finally, no separate treatment of the point-to-point correlated systematic uncertainties was performed at that time, because it was assumed that it would move all points in the same direction (positive correlation) and thus have no impact on the measured $\langle p_{\mathrm{T}}^2 \rangle$.

The data, within uncertainties, include the possibility of a modest broadening of the transverse momentum distribution relative to $p + p$ collisions. This is often attributed to initial- and final-state multiple scattering, sometimes referred to as the "Cronin effect." However, in calculating $\Delta\langle p_{\mathrm{T}}^2 \rangle = \langle p_{\mathrm{T}}^2 \rangle_{d\mathrm{Au}} - \langle p_{\mathrm{T}}^2 \rangle_{pp}$ one finds that this effect needs reduced uncertainties from future larger data sets to make any firm conclusions.

Figure 4 shows the J/ψ invariant yield, integrated over all p_{T}, as a function of rapidity for d + Au collisions. Shown are the results of the new analysis presented in this paper, as well as the previously published results [4] using the same data set. Overall the agreement of the two analysis results is good. The two sets of points differ in the reconstruction software, analysis cuts, and signal-extraction technique. Thus many of the systematic uncertainties are different, and even the statistical uncertainties are not identical owing to the different analysis cuts and the use of event mixing to estimate the combinatorial background in the new analysis, as opposed to the like-sign mass distribution used in Ref. [4].

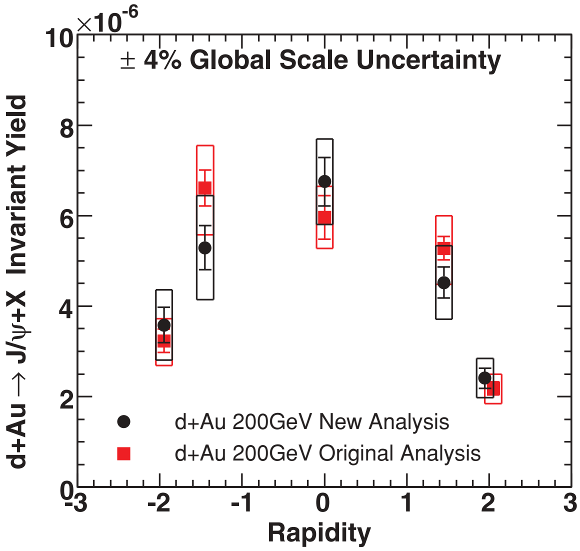

FIG. 4. (Color online) J/ψ invariant yield as a function of rapidity for d + Au collisions. Shown are the new analysis results from this paper, in addition to the originally published results [4] using the same data. The global systematic uncertainty quoted is for the new analysis.

Figure 5 shows the J/ψ invariant yield for $p + p$ collisions, from both the published high-statistics result from Run-5 [2], as well as the lower statistics result from Run-3 as published in Ref. [4]. In both cases the points are in good agreement within the systematic uncertainty bands. A new analysis of the Run-3 $p + p$ lower statistics data set was also performed by using the same technique and analysis cuts as for d + Au collisions. It also shows good agreement with these two sets of measurements, albeit with larger statistical uncertainties.

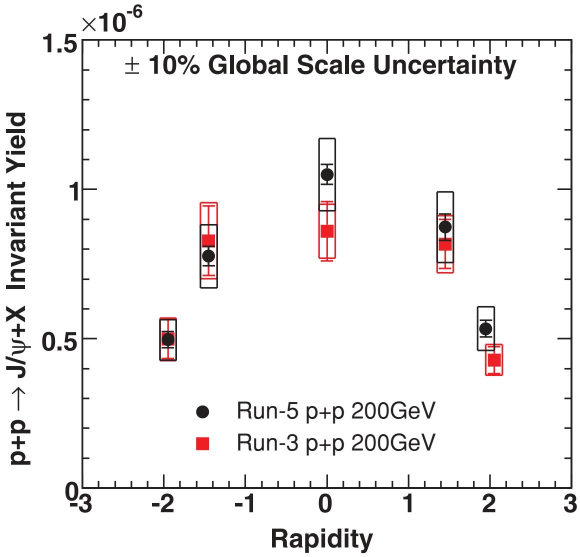

FIG. 5. (Color online) J/ψ invariant yield as a function of rapidity for $p + p$ collisions. Shown are the high statistics results from the 2005 $p + p$ PHENIX data-taking period [2] and the originally published results [4] using the 2003 $p + p$ data set. The global systematic uncertainty quoted is for the new analysis.

In Figs. 4 and 5, the highest rapidity point is not located exactly at the same rapidity position between the original and the new analysis. This is because the positive-rapidity muon arm has a slightly larger rapidity coverage than the negative-rapidity arm. This property was used in the 2003 analysis to include additional J/ψ mesons at forward rapidity to probe a slightly lower region of x. It was found, however, that there were very few counts in this region and that the asymmetric rapidity range created additional difficulties when comparing the results measured at forward and backward rapidity (in case of symmetric collisions) and when comparing the results obtained in $p + p$ collisions to Cu + Cu or Au + Au collisions, for which this extra rapidity coverage was not available (because of high-occupancy limitations at forward rapidity). As a consequence, it was decided for the later analyses to forgo the extra few J/ψ counts at very forward rapidity and use the same-width rapidity bins at both positive and negative rapidity.

V. NUCLEAR MODIFICATION FACTOR

The J/ψ nuclear modification factor in a given centrality and rapidity bin is

$$R_{d\mathrm{Au}} = \frac{1}{\langle N_{\mathrm{coll}}\rangle} \frac{dN^{d+\mathrm{Au}}_{J/\psi}/dy}{dN^{p+p}_{J/\psi}/dy}, \qquad (3)$$

where $dN^{d\mathrm{Au}}_{J/\psi}/dy$ is the J/ψ invariant yield measured in $d +$ Au collisions, $dN^{pp}_{J/\psi}/dy$ is the J/ψ invariant yield measured in $p + p$ collisions for the same rapidity bin, and $\langle N_{\mathrm{coll}}\rangle$ is the average number of binary collisions in the centrality bin under consideration, as listed in Table I. All $R_{d\mathrm{Au}}$ values as a function of p_T, y, and centrality including statistical and systematic uncertainties are given in Table II.

Figure 6 shows the nuclear modification factor $R_{d\mathrm{Au}}$ calculated by using the $d +$ Au new analysis presented in this paper for the numerator and the 2005 $p + p$ data for the denominator. In contrast to the previous analysis [4], where the $p + p$ results were symmetrized around $y = 0$ before calculating $R_{d\mathrm{Au}}$ to compensate for lower J/ψ statistics in the 2003 $p + p$ data set, in this case the $R_{d\mathrm{Au}}$ values are calculated independently at each rapidity.

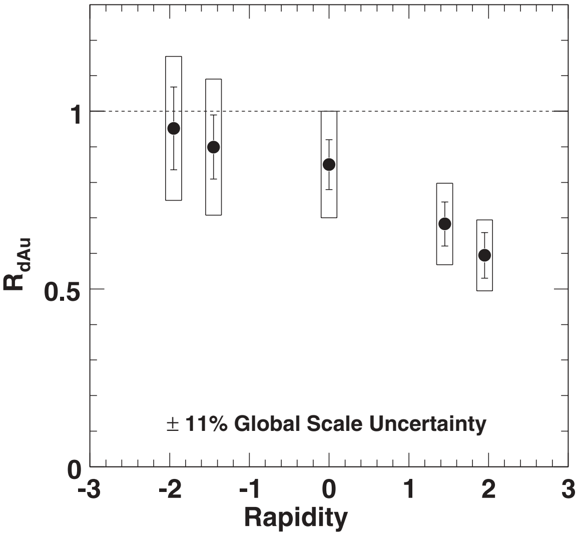

FIG. 6. J/ψ nuclear modification factor $R_{d\mathrm{Au}}$ as a function of rapidity.

The understanding of the detector performance in terms of alignment, resolution, and efficiency has significantly improved between this analysis and previously published PHENIX $d +$ Au results [4]. This resulted in changes in the reconstruction software, analysis cuts, signal-extraction technique, and handling of both the physical and combinatorial background in the dilepton invariant mass distribution. Simultaneously, the systematic uncertainties associated with the measurement have also been reevaluated in a way consistent with what was learned for the $p + p$, Cu + Cu, and Au + Au analyses. The new uncertainties are in general larger, although some of them cancel with their $p + p$ counterpart when forming $R_{d\mathrm{Au}}$. This approximately counterbalances the reduction of the statistical uncertainty achieved by using the 2005 $p + p$ data set as a reference. Additionally, the J/ψ production cross sections in $p + p$ collisions measured in 2005 [2] are compatible within uncertainties but higher than the values used in Ref. [4] (based on the 2003 $p + p$ data set) by about 13%. As a consequence, the new nuclear modification factors are systematically lower than the ones previously published by about 5–20% for most points, depending on the p_{T}, y, or centrality bin considered.

Within uncertainties, the nuclear modification factors are consistent with $R_{d\mathrm{Au}} = 1.0$ at negative and midrapidities and are significantly lower than 1.0 at forward rapidity only, that is, in the deuteron-going direction. This trend is similar to that shown in Fig. 1 of Ref. [4], although the new values are systematically smaller for all rapidity bins.

Figure 7 shows the J/ψ nuclear modification factor in $d +$ Au collisions as a function of the number of binary collisions for three rapidity ranges and four centrality classes. Only at forward rapidity is there statistically significant suppression.

VI. DISCUSSION

As stated in the Introduction, the $d +$ Au data are interesting both to fundamentally understand issues of quarkonia and cold nuclear matter and also to separate these effects from hot nuclear matter effects in heavy-ion collisions. To address both issues, we compare the experimental data with two different models including both modification of the initial parton distribution functions (PDFs) and a free parameter to account for the breakup of correlated $c\bar{c}$ pairs that might have otherwise formed J/ψ mesons. Note that, often in the literature, this breakup process in cold nuclear matter is referred to as an absorption cross section of the J/ψ particles on the nucleons in the nucleus. Here we avoid this nomenclature, both because the object that is “absorbed” is generally not a fully formed J/ψ but rather a $c\bar{c}$ pair, and because the actual process is more a breakup of this pair, rather than the absorption of it.

Shown in Fig. 8 is the nuclear modification factor $R_{d\mathrm{Au}}$ as a function of rapidity in comparison to theoretical calculations [3] that include either EKS [12] or NDSG [13] shadowing

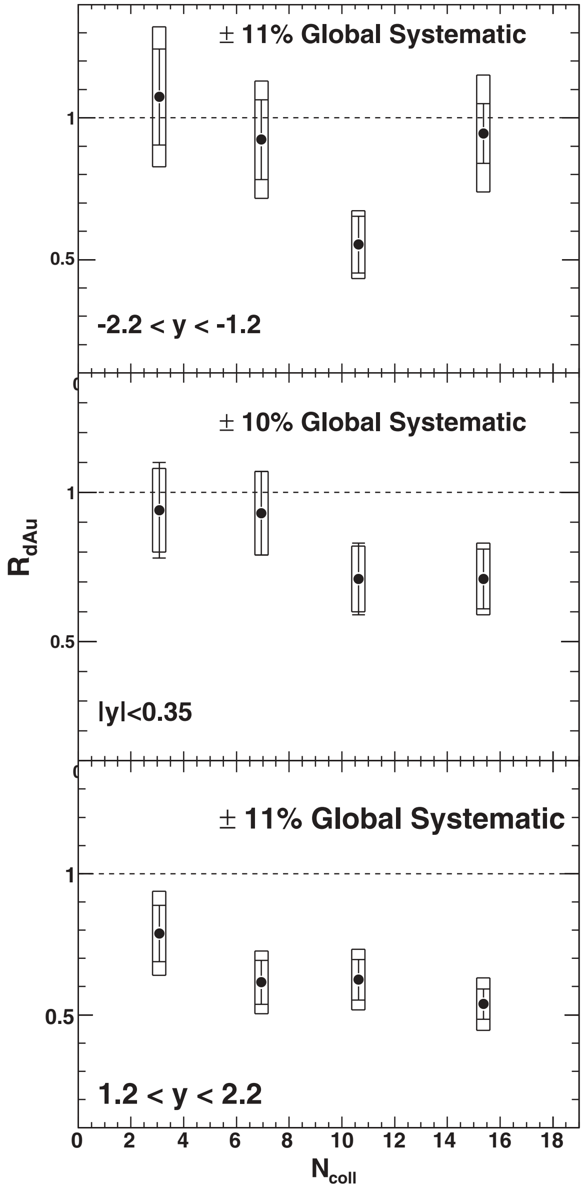

FIG. 7. J/ψ nuclear modification factor $R_{d\mathrm{Au}}$ as a function of N_{coll} for three rapidity ranges.

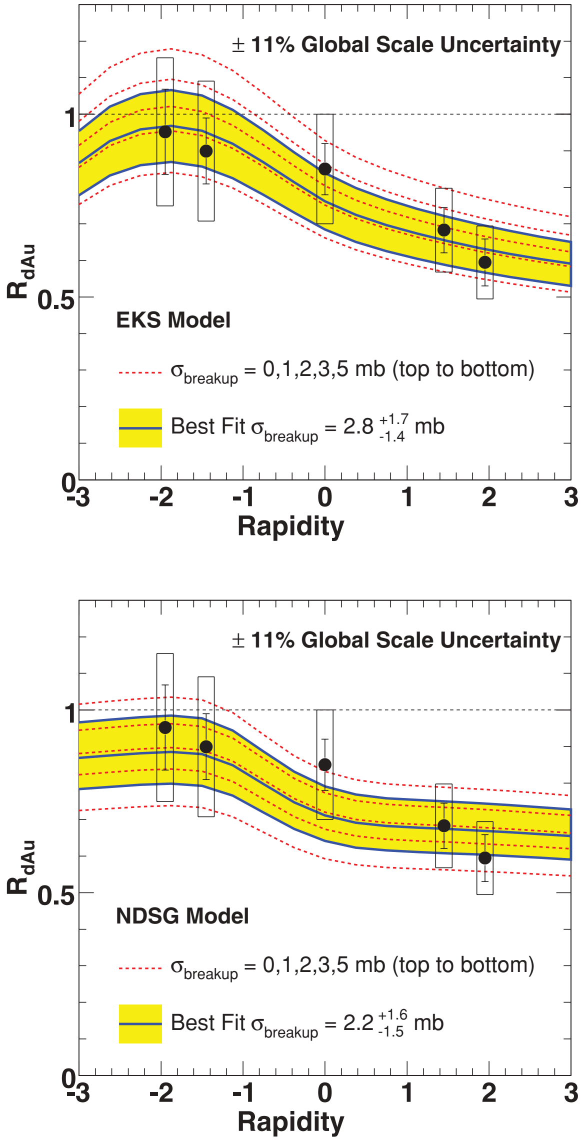

FIG. 8. (Color online) $R_{d\mathrm{Au}}$ data compared to various theoretical curves for different $\sigma_{\mathrm{breakup}}$ values. Also shown as a band are the range of $\sigma_{\mathrm{breakup}}$ values found to be consistent with the data within one standard deviation. The top panel is a comparison for EKS shadowing [12]; the bottom panel is for NDSG shadowing [13].

models for the nuclear PDFs. In each case an additional suppression associated with a $\sigma_{\mathrm{breakup}}$ is also included. Note that there is no *ab initio* calculation of this cross section, and although one might expect a similar value to results at lower energy [14], it need not be identical.

Taking full account of the statistical and systematic uncertainties on the experimental data, we can determine the breakup cross section under certain assumptions. We have followed the statistical procedure detailed in Ref. [15]. If we assume that the EKS-modified nuclear PDFs are exactly correct, and that the only additional suppression is accounted for by $\sigma_{\mathrm{breakup}}$, then the data constrain $\sigma_{\mathrm{breakup}} = 2.8^{+1.7}_{-1.4}$ mb with the uncertainties as one standard deviation. Similarly, if we assume the NDSG-modified nuclear PDFs, then we obtain $\sigma_{\mathrm{breakup}} = 2.2^{+1.6}_{-1.5}$ mb. These breakup cross-section values are consistent (within the large uncertainties) with the 4.2 ± 0.5 mb value determined at lower energies at the CERN-SPS [14]. The extracted breakup cross section at lower energies are found by assuming no contribution from the modification of nuclear PDFs. At the lower energies, J/ψ production is sensitive to higher x partons in the antishadowing regime where the modifications are expected to be smaller and in the opposite direction [16].

The modified nuclear PDFs from EKS and NDSG are constrained from other experimental measurements such as deep inelastic scattering from various nuclear targets and the resulting $F_2(A)$ structure functions. A geometric parametrization of these PDFs based on the path of the parton through the nucleus is described in Refs. [17] and [3]. One can test this geometric dependence by comparison with the $d+\mathrm{Au}$ nuclear modification factors as a function of N_{coll}. Using this

TABLE V. Most probable values and one standard deviations of $\sigma_{\mathrm{breakup}}$ determined by assuming two different shadowing models, from a fit to minimum-bias $R_{d\mathrm{Au}}$ points as a function of rapidity (Fig. 8), and fits to $R_{d\mathrm{Au}}$ as a function of N_{coll} in three separate rapidity bins (Fig. 9).

Fit range in y	EKS (mb)	NDSG (mb)
All	$2.8^{+1.7}_{-1.4}$	$2.2^{+1.6}_{-1.5}$
[−2.2, −1.2]	$5.2^{+1.6}_{-1.8}$	$3.3^{+2.0}_{-1.7}$
[−0.35, 0.35]	$2.4^{+1.9}_{-1.6}$	$1.0^{+1.8}_{-1.7}$
[1.2, 2.2]	$3.2^{+1.6}_{-1.5}$	$3.3^{+1.5}_{-1.5}$

geometric dependence, we can calculate the most probable $\sigma_{\mathrm{breakup}}$ values independently in three rapidity ranges (see Table V). The corresponding nuclear modification values and their one-standard-deviation bands are shown as a function of N_{coll} in Fig. 9. The two calculations with EKS and NDSG nuclear PDFs yield almost identical bands since the same geometric dependence is used in both cases. However, each band represents a different balance of modification owing to the nuclear PDF and the breakup cross section.

For both the EKS and the NDSG PDFs, the values of $\sigma_{\mathrm{breakup}}$ extracted from the overall rapidity dependence of $R_{d\mathrm{Au}}$ and from the N_{coll} dependence of $R_{d\mathrm{Au}}$ within the different rapidity ranges are consistent within the large systematic uncertainties. It should be noted that though the confidence level for the best fit is poor at backward rapidity (as can be seen in Fig. 9), there is still a well-defined maximum in the likelihood function for $\sigma_{\mathrm{breakup}}$. A future higher precision $R_{d\mathrm{Au}}$ measurement as a function of centrality will be crucial to constrain the exact geometric dependence.

One can also utilize this model to do a consistent calculation of the contribution from cold nuclear matter effects that should be present in Cu + Cu and Au + Au collisions. These contributions, obtained using the best-fit value of $\sigma_{\mathrm{breakup}}$ and their one-standard-deviation values extracted from the data in Fig. 8 for each of the two shadowing models, are shown in Figs. 10 and 11. In the Cu + Cu case, J/ψ production is not suppressed beyond cold nuclear matter effects at midrapidity or at forward rapidity, within the limits of the large error bands, and the midrapidity data in the Au + Au case are similarly inconclusive. However, there is a significant suppression in the data at forward rapidity, beyond the uncertainties in both the data and the projection. It should be noted that the uncertainty bands at forward rapidity and midrapidity are entirely correlated, as they reflect only the uncertainty in $\sigma_{\mathrm{breakup}}$. There is no systematic uncertainty included for the choice of modified nuclear PDF model, which is the only way to change the relative suppression between forward rapidity and midrapidity within the context of this calculation. The more data-driven calculation described later in this section, however, is performed independently at different rapidities and does not suffer the same stipulation.

It should also be noted that the theoretical calculations yield R_{AA} as a continuous function of the number of participants, whereas the data points are at discrete values representing a convolution of the modification factor with the N_{part} distribution within a particular centrality category. A Glauber simulation combined with a Monte Carlo simulation of the PHENIX experimental trigger and centrality selection is utilized to convert the continuous theory predictions into discrete predictions in the simulated PHENIX centrality categories. Thus, the results shown in the figures are in fact predictions for the matched event selection categories of the experimental data points.

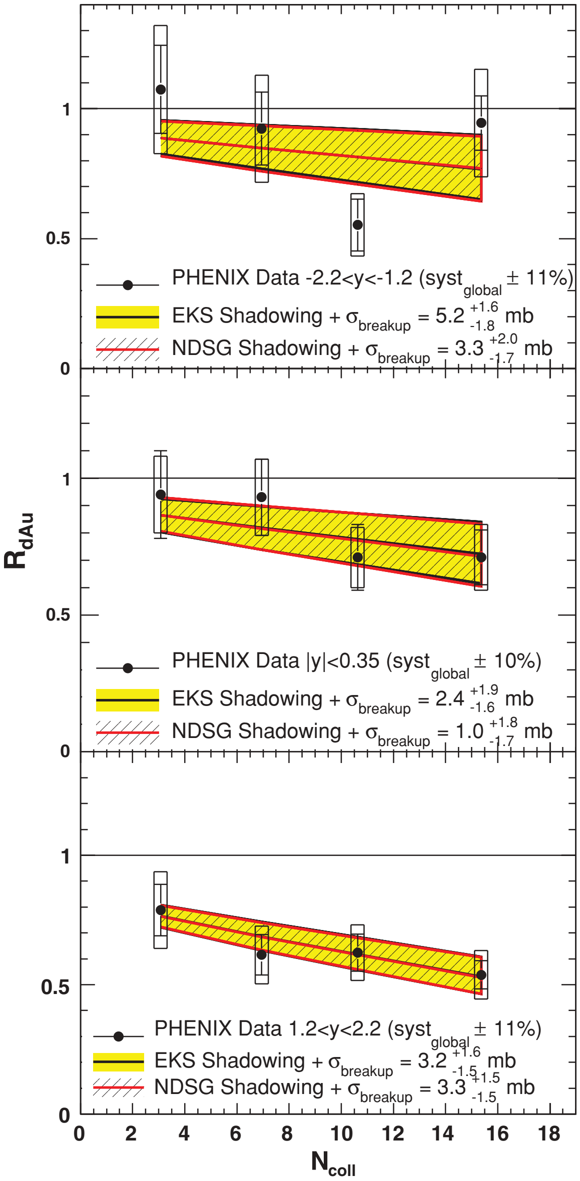

FIG. 9. (Color online) $R_{d\mathrm{Au}}$ data as a function of N_{coll} for three different rapidity ranges. Overlayed are theoretical curves representing the best-fit $\sigma_{\mathrm{breakup}}$ values as determined in each rapidity range separately, utilizing EKS and NDSG nuclear PDFs and a simple geometric dependence. Also shown as bands are the range of $\sigma_{\mathrm{breakup}}$ values found to be consistent with the data within one standard deviation.

To explore the cold nuclear matter constraints further, an alternative data-driven method proposed in Ref. [18] is

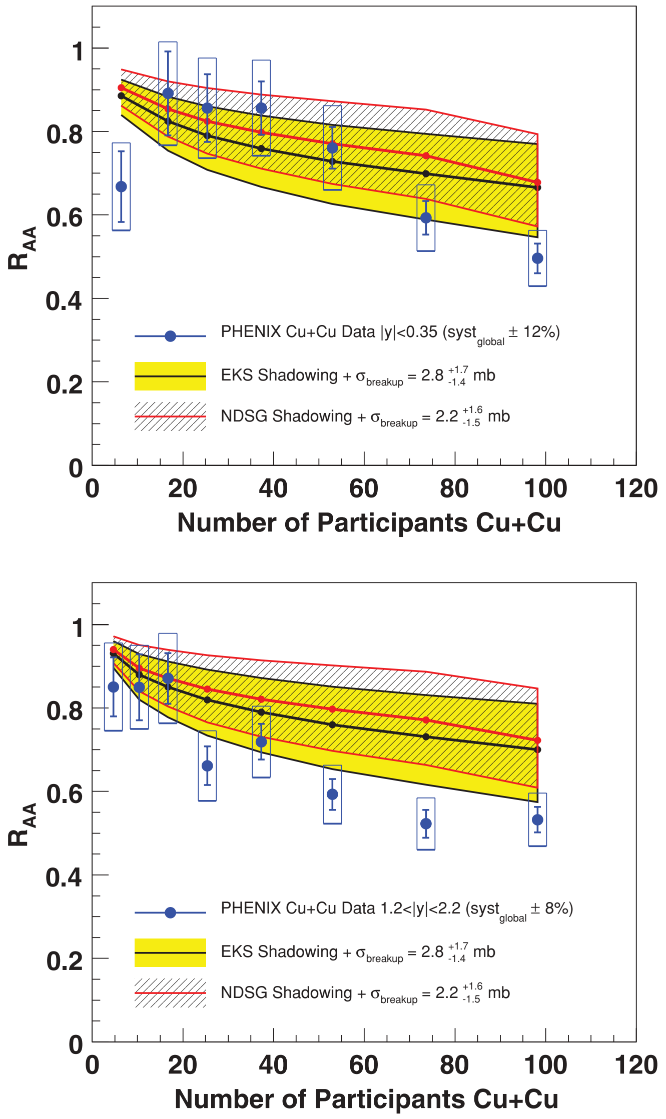

FIG. 10. (Color online) R_{AA} for Cu + Cu [5] collisions compared to a band of theoretical curves for the σ_{breakup} values found to be consistent with the d + Au data as shown in Fig. 8. The top figure includes both EKS shadowing [12] and NDSG shadowing [13] at midrapidity. The bottom figure is the same at forward rapidity.

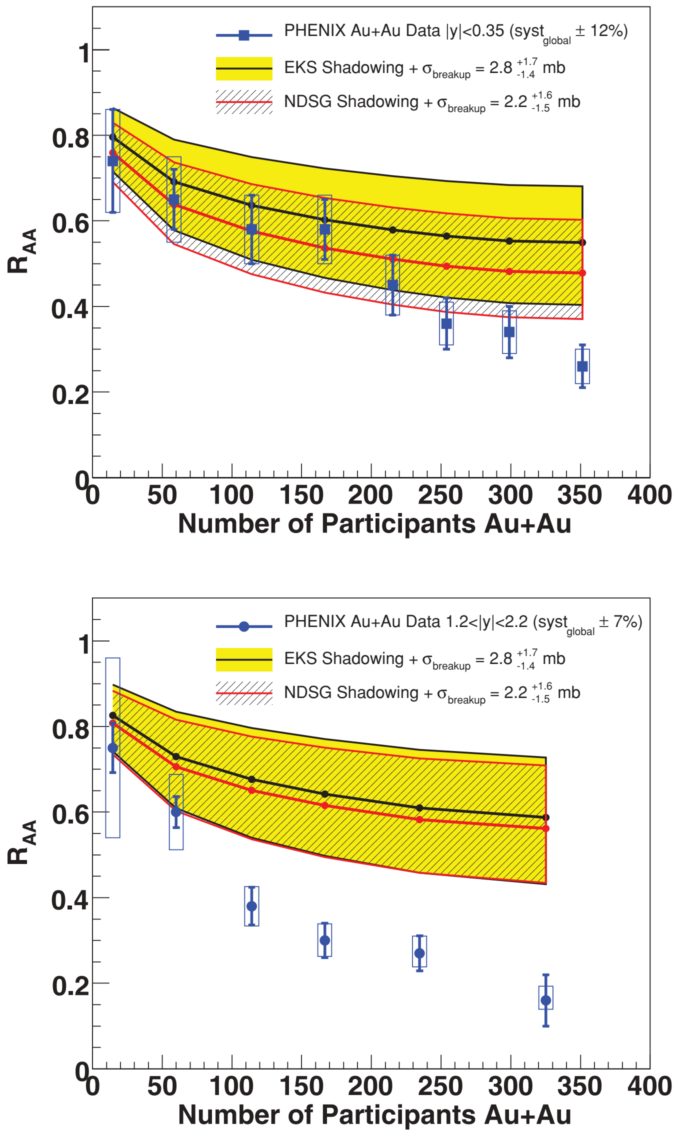

FIG. 11. (Color online) R_{AA} for Au + Au [1] collisions compared to a band of theoretical curves for the σ_{breakup} values found to be consistent with the d + Au data as shown in Fig. 8. The top figure includes both EKS shadowing [12] and NDSG shadowing [13] at midrapidity. The bottom figure is the same at forward rapidity.

used. In this approach it is assumed that there is a single modification factor parametrizing all cold nuclear matter effects that is a simple function of the radial position in the nucleus. This computation has the advantage of our not having to assume a specific shadowing scheme and a specific breakup cross section, but instead relies only on the measured impact parameter dependence. The cold nuclear matter effects suffered by a J/ψ in a Au + Au collision at a given rapidity are assumed to be the product of the modifications measured in d + Au collisions at the same rapidity and the modifications measured at the opposite rapidity (or, equivalently, in a Au + d collision). This assumption holds for the two effects considered so far, namely, shadowing and subsequent breakup. In the computation it is also assumed that the same parton distributions are sampled by the J/ψ particles observed in the (wide) rapidity range in Au + Au and d + Au collisions. Note that since this model implicitly includes any possible modified nuclear PDFs, the modification factors may have an x dependence that is accounted for by considering the backward, mid, and forward rapidity d + Au data. The different rapidity regions are sensitive to the initial-state partons in the gold nucleus in three broad ranges of x, corresponding to $x \approx$ 0.002–0.01, 0.01–0.05, and 0.05–0.2, as determined from PYTHIA.

A Glauber Monte Carlo simulation and a simulation of the BBC detector used for centrality determination and triggering are done. The resulting four centrality categories (0–20%, 20–40%, 40–60%, and 60–88%) in d + Au collisions are characterized by a distribution in the number of binary collisions, as shown in the top panel of Fig. 12. In addition,

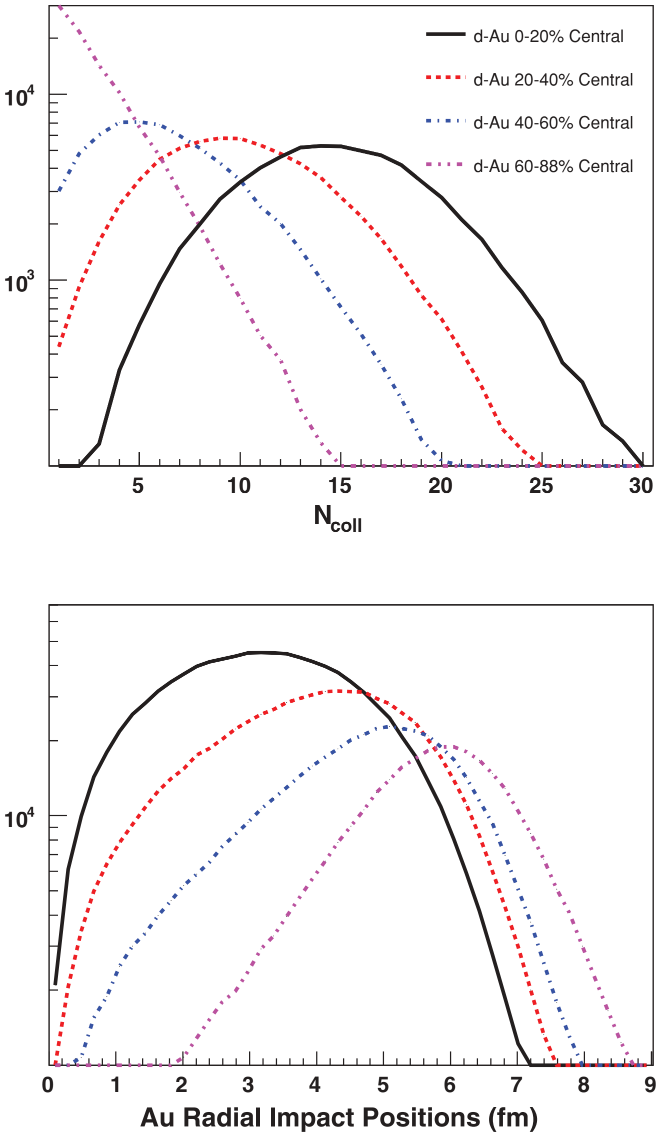

FIG. 12. (Color online) Results from a Glauber model Monte Carlo simulation of the $d +$ Au centrality selection and triggering based on the PHENIX BBC. The top panel shows the distribution of the number of binary collisions for events in each of the four centrality classes 0–20%, 20–40%, 40–60%, and 60–88%. The distribution for radial impact points in the gold nucleus of binary collisions is shown in the lower panel.

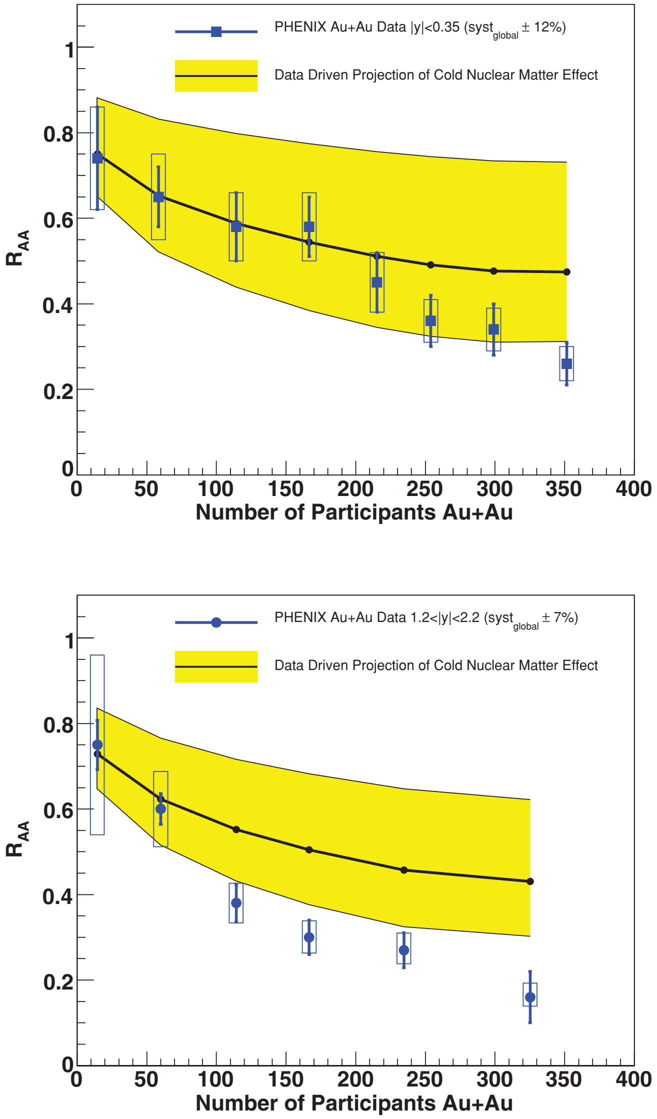

FIG. 13. (Color online) Predictions of the data-driven method [18] constrained by $R_{d\mathrm{Au}}$ as a function of collision centrality for the Au + Au R_{AA} for midrapidity (top) and at forward rapidity (bottom).

the distribution of radial positions r in the Au nucleus of binary collisions is calculated and shown in the bottom panel of Fig. 12.

The procedure is to use the forward, mid, and backward rapidity centrality-dependent $R_{d\mathrm{Au}}$ values to constrain the modification factor $\Re(r)$ for three broad regions of initial parton x ($\Re_{\mathrm{low}}$, $\Re_{\mathrm{mid}}$, and $\Re_{\mathrm{high}}$, respectively). Then one can use these parametrizations to project the cold nuclear matter effect in the Au + Au case. The current $d +$ Au data are insufficient to constrain the functional form of $\Re(r)$. As a simplifying case, $\Re(r)$ is assumed to be linear in r and to be fixed at $\Re(r \geqslant 8\,\mathrm{fm}) = 1.0$ at the edge of the gold nucleus. Thus, the only free parameter is the slope (or, equivalently, the magnitude of the modification factor at $r = 0$). Other functions were tried and essentially differ by their extrapolation to lower and higher radial positions, because the data are not precise enough to constrain the shape. This has a particularly strong impact on the most peripheral collisions for which our assumption that $\Re(r \geqslant 8\,\mathrm{fm}) = 1.0$ adds a significant constraint to the shape.

For all possible slope parameters, consistency with the experimental data is checked by using the procedure detailed in Ref. [15], which utilizes the full statistical and systematic uncertainties. The range of parameters within one standard deviation of the uncertainties is determined separately for backward, mid, and forward rapidity. Using this range of parameters, we can project the cold nuclear matter suppression expected in Au + Au collisions as a function of collision centrality and for midrapidity and forward rapidity. Note that the forward rapidity Au + Au J/ψ production is sensitive to the low-x partons in one gold nucleus and the high-x

partons in the other gold nucleus. Thus, in the Monte Carlo simulation, for every binary collision at r_1 and r_2 (the radii with respect to the center of each nucleus) the expected modification is $\Re_{\mathrm{low}}(r_1) \times \Re_{\mathrm{high}}(r_2)$. The midrapidity Au + Au J/ψ production is predominantly sensitive to the mid-x partons from both gold nuclei and therefore the expected modification is $\Re_{\mathrm{mid}}(r_1) \times \Re_{\mathrm{mid}}(r_2)$. The total modification expected is calculated by taking the average over all correlated r_1 and r_2 positions for binary collisions within overall Au + Au collisions in each Au + Au centrality class.

The results of these calculations matched to the experimentally measured Au + Au centrality bins are shown in Fig. 13. It is notable that the midrapidity cold nuclear matter extrapolation agrees within the uncertainty of the experimental data at midrapidity. Thus, it is not possible within the current constraints to determine the potential extent of hot nuclear matter effects. This conclusion is qualitatively similar to that reached from the previous model calculations as shown in Fig. 11. However, at forward rapidity, this method projects a somewhat larger range of possible cold nuclear matter effects than the previous models.

Neither the predictions of cold nuclear matter effects in heavy-ion collisions based on fitting of the d + Au data with theoretical curves (Figs. 10 and 11) nor those obtained directly from the d + Au data points (Fig. 13) are well-enough constrained to permit quantitative conclusions about additional hot nuclear matter effects.

VII. CONCLUSIONS

A new analysis of J/ψ production in d + Au collisions at $\sqrt{s_{NN}} = 200$ GeV has been presented using the PHENIX 2003 d + Au data set. Cuts and analysis techniques that are consistent with the previously published results for $p + p$, Cu + Cu, and Au + Au collisions at the same energy [1,2,5] are used. The new analysis also benefits from the significantly larger $p + p$ data set from Run-5.

A statistical comparison of these new results to theoretical calculations has been performed with a detailed handling of the experimental uncertainties to estimate a J/ψ (or precursor) breakup cross section in cold nuclear matter on top of models for the modifications of the parton distribution functions in the nucleus. Using EKS (NDSG) shadowing, we obtain a breakup cross section of $2.8^{+1.7}_{-1.4}$ ($2.2^{+1.6}_{-1.5}$) mb. These breakup cross-section values are consistent within large uncertainties with the 4.2 ± 0.5 mb determined at lower energies at the CERN-SPS [14]. The measured values are then used to predict the expected cold nuclear matter effects on J/ψ production in Cu + Cu and Au + Au collisions, and these are compared to the measured nuclear modification factors for those systems. These predictions are found to be similar to those from a less model-dependent and more data-driven method based on the variation of the nuclear modification factor measured in d + Au collisions as a function of both rapidity and centrality [18]. It is notable that the latter method yields a somewhat larger possible suppression in the forward rapidity case. In all cases the large error bars associated with the extrapolation prevent us from making firm quantitative statements on any additional J/ψ suppression in Au + Au collisions beyond that expected from cold nuclear matter effects. A d + Au data set with much improved statistical precision is needed to both reduce the statistical uncertainties and permit better control over the systematic uncertainties.

ACKNOWLEDGMENTS

We thank the staff of the Collider-Accelerator and Physics Departments at Brookhaven National Laboratory and the staff of the other PHENIX participating institutions for their vital contributions. We also thank Ramona Vogt for useful discussions and for the calculations used to set the level of the breakup cross sections. We acknowledge support from the Office of Nuclear Physics in the Office of Science of the Department of Energy, the National Science Foundation, Abilene Christian University Research Council, Research Foundation of SUNY, and the Dean of the College of Arts and Sciences, Vanderbilt University (U.S.A.), Ministry of Education, Culture, Sports, Science, and Technology and the Japan Society for the Promotion of Science (Japan), Conselho Nacional de Desenvolvimento Científico e Tecnológico and Fundação de Amparo à Pesquisa do Estado de São Paulo (Brazil), Natural Science Foundation of China (People's Republic of China), Ministry of Education, Youth and Sports (Czech Republic), Centre National de la Recherche Scientifique, Commissariat à l'Énergie Atomique, and Institut National de Physique Nucléaire et de Physique des Particules (France), Ministry of Industry, Science and Tekhnologies, Bundesministerium für Bildung und Forschung, Deutscher Akademischer Austausch Dienst, and Alexander von Humboldt Stiftung (Germany), Hungarian National Science Fund, OTKA (Hungary), Department of Atomic Energy (India), Israel Science Foundation (Israel), Korea Research Foundation and Korea Science and Engineering Foundation (Korea), Ministry of Education and Science, Russia Academy of Sciences, Federal Agency of Atomic Energy (Russia), VR and the Wallenberg Foundation (Sweden), the U.S. Civilian Research and Development Foundation for the Independent States of the Former Soviet Union, the US-Hungarian NSF-OTKA-MTA, and the US-Israel Binational Science Foundation.

---

[1] A. Adare *et al.*, Phys. Rev. Lett. **98**, 232301 (2007).
[2] A. Adare *et al.*, Phys. Rev. Lett. **98**, 232002 (2007).
[3] R. Vogt, Phys. Rev. C **71**, 054902 (2005).
[4] S. S. Adler *et al.*, Phys. Rev. Lett. **96**, 012304 (2006).
[5] A. Adare *et al.*, arXiv:0801.0220 [nucl-ex].
[6] K. Adcox *et al.*, Nucl. Instrum. Methods A **499**, 469 (2003).
[7] S. N. White, AIP Conf. Proc. **792**, 527 (2005).
[8] M. L. Miller, K. Reygers, S. J. Sanders, and P. Steinberg, Ann. Rev. Nucl. Part. Sci. **57**, 205 (2007).
[9] A. Spiridonov, arXiv:hep-ex/0510076 (2004).
[10] *GEANT 3.2.1 Manual* (CERN, Geneva, 1993); available at http://wwwasdoc.web.cern.ch/wwwasdoc/pdfdir/geant.pdf.

[11] Torbjorn Sjöstrand, Stephen Mrenna, and Peter Skands, PYTHIA 6.4 physics and manual, JHEP 05 (2005) 026 [also hep-ph/0603175].

[12] K. J. Eskola, V. J. Kolhinen, and R. Vogt, Nucl. Phys. **A696**, 729 (2001).

[13] D. deFlorian and R. Sassot, Phys. Rev. D **69**, 074028 (2004).

[14] B. Alessandro *et al*., Eur. Phys. J. C **48**, 329 (2006).

[15] A. Adare *et al*., arXiv:0801.1665 [nucl-ex].

[16] C. Lourenco, Nucl. Phys. **A783**, 451 (2007).

[17] S. R. Klein and R. Vogt, Phys. Rev. Lett. **91**, 142301 (2003).

[18] R. Granier de Cassagnac, J. Phys. G **34**, S955 (2007).